Surface & Coatings Technology 374 (2019) 634–644

Contents lists available at ScienceDirect

Surface & Coatings Technology

journal homepage: www.elsevier.com/locate/surfcoat

An experimental study to characterize a surface treated with a novel laser surface texturing technique: Water repellency and reduced ice adhesion

Yang Liu[a], Zichen Zhang[a], Haiyang Hu[a], Hui Hu[a,*], Avik Samanta[b], Qinghua Wang[b], Hongtao Ding[b]

[a] Department of Aerospace Engineering, Iowa State University, 2271 Howe Hall, Room 1200, Ames, IA 50011, USA
[b] Department of Mechanical Engineering, University of Iowa, Iowa City, IA, 52242, USA

ARTICLE INFO

Keywords:
Laser surface nanostructuring
Wettability and icephobicity
Water droplet impingement
Ice adhesion strength

ABSTRACT

An experimental study was conducted to characterize the laser-textured surfaces fabricated by using a novel nanosecond Laser-based High-throughput Surface Nanostructuring (*n*HSN) method. While the two-step *n*HSN approach (i.e., water-confined nanosecond laser texturing and chemical immersion treatment) in producing superhydrophobicity over metal surfaces is described in great details, a throughput analysis of different laser-based surface texturing methods is also performed in the term of Specific Laser Scanning Time (SLST). It is found that the *n*HSN process significantly increases the processing rate from hundreds of minutes per square inch to seconds in comparison to the existing ultrashort laser-based surface texturing techniques. In order to examine the performance of the novel *n*HSN-treated surfaces in the term of "water-/ice-repellency", a series of experiments were performed in the present study to not only characterize the surface structures and wettability of the *n*HSN-treated aluminum surfaces, but also evaluate the effects of the *n*HSN treatment on the dynamics of water droplet during the impacting process (i.e., spreading, receding, and rebounding), as well as their capability in reducing ice adhesion strength. It is found that, while the untreated bare aluminum surface and the only laser-textured aluminum surface are hydrophilic with the static contact angle being smaller than 90° and the contact angle hysteresis being larger than 90°, the *n*HSN-treated surfaces appear to be superhydrophobic with a significantly larger static contact angle (i.e., ~170°) and a much smaller contact angle hysteresis (i.e., ~20°). The super-hydrophobicity of the *n*HSN surfaces is further promoted to "ice-repellency" by the complete droplet rebounding phenomenon in the dynamic water droplet impacting process and the reduced ice adhesion strength.

1. Introduction

Water corrosion and Ice formation are commonly observed on various engineering structures such as heat exchangers, power transmission lines, bridge cables, aircraft wings, and wind turbines [1–4]. The water deposition or ice formation on the exposed surfaces of the engineering structures would significantly degrade the operational performance and may cause serious safety issues. In addition, extra energy is usually required to remove the corrosive water or accreted ice on these surfaces, which can lead to a large amount of energy consumption in their daily operations [5]. To solve these problems, various techniques have been developed over the past decades, which can be categorized into either passive or active approaches. While passive anti-icing strategies are mainly dependent on the utilization of specialized hydro- and ice-phobic coatings/materials, active anti-/de-icing methods usually require energy expenditure [6]. As an effective evaporating/melting mechanism, electro-thermal systems have been widely used to evaporate deposited water or melt out ice by heating up the various engineering surfaces [7–9]. However, they are usually very inefficient and have demanding power requirements. Thus, the passive water-/ice-repellency methods, especially the hydro-/ice-phobic coatings/surfaces, have become the most favorable candidate for the mitigation of water corrosion and ice accretion on various engineering structures.

Over the past decades, extensive studies have been conducted to develop super-hydrophobic surfaces/coatings, as inspired by the exceptional water-repellency phenomena found in nature, e.g., lotus leaves and duck feathers. Super-hydrophobic surfaces are featured by their outstanding self-cleaning capabilities, on which water droplets have a very large contact angle (i.e., usually larger than 150°), and could drop off rapidly over the surface with an inclined angle. In addition to the extraordinary water-repellency, the super-hydrophobic

* Corresponding author.
E-mail address: huhui@iastate.edu (H. Hu).

https://doi.org/10.1016/j.surfcoat.2019.06.046
Received 26 March 2019; Received in revised form 13 June 2019; Accepted 15 June 2019
Available online 17 June 2019
0257-8972/

surfaces draw more attentions in recent years due to their potential to reduce ice/snow accumulation over solid surfaces. It was suggested that some superhydrophobic surfaces reduce ice adhesion strength and delay ice formation under a frost-free environment [10] at subzero temperatures. Among the various methods to fabricate super-hydrophobic surfaces, laser-based surface texturing techniques are emerging as a promising approach due to their unique advantages in precisely controlling the feature size, reduced processing time, and compatibility to different materials. In recent years, extensive efforts have been made to make hydrophobic surfaces using ultrashort lasers, e.g. femtosecond and picosecond lasers. Bizi-Bandoki et al. [11] modified the surface topography and wetting properties of steel and titanium alloy via femtosecond laser processing. The contact angle (CA) of water on the laser-treated surface was found to increase as the pulse density was increased. Cunha et al. [12] obtained four types of femtosecond laser textured T-6Al-4V surfaces and highlighted the importance of anisotropy of the surfaces in controlling the wetting behavior. Rukosuyev et al. [13] developed a one-step fabrication method for super-hydrophobic surfaces using femtosecond laser with no post chemical treatment. It was revealed that the hydrophobic behavior of the laser-treated surface was mainly attributed to the surface structures obtained by the femtosecond laser ablation, but regardless of the surface properties of base material. Vorobyev and Guo [14] produced hierarchical nano-/micro-structures over multifunctional surfaces using a femtosecond laser, which also exhibited superhydrophobicity and evident self-clean effect. Jagdheesh et al. [15] machined microchannels and micropillars by using a nanosecond laser, which were suggested to be the key structures promoting the hydrophobic surface. By depositing a thin amorphous carbon (a-C) film on the laser-textured stainless steel surface, Luo et al. [16] further increased the hydrophobicity of the surface in comparison to the laser textured surface without the chemical treatment. Kwon et al. [17] fabricated micro pillar arrays on a stainless steel surface with deposited re-entrant structure of copper via laser ablation, insulating, mechanical polishing and electrodeposition. The results demonstrated that the hydrophobicity of the surface is largely determined by the spacing of the micro-pillars in the arrays. Carpeño et al. [18] deposited nickel thin films on Ti6Al4V and laser treated the films using a nanosecond pulse ultraviolet laser. Three different micro- and nano-levels of roughness were generated on the film surface which led to the increase of CA. Silanization was extensively applied as a fast and convenient surface chemistry transition method for laser textured surfaces of steel [19,20], aluminum alloy [21] and titanium [22]. By lowering the surface energy on these laser-textured surfaces, the hydrophobicity was significantly improved. Chun et al. [23] used low temperature annealing and ethanol to rapidly transit the wettability of copper oxide. With these post-treatment processes, the efficiency of these laser-based fabrication methods in producing hydrophobic surfaces was greatly improved.

While a number of laser-based surface texturing methods have been demonstrated to be able to produce superhydrophobic surfaces, they are usually very time-consuming (i.e., up to days or months) and sometimes not feasible in processing large area samples. In the present study, a novel nanosecond laser-based high-throughput surface nanostructuring (*n*HSN) [24–26] approach is introduced, which can produce superhydrophobic surfaces over various metal alloys with a much higher efficiency in achieving large area processing for practical throughput. It should be noted that, while superhydrophobic surfaces are considered to be able to reduce/prevent ice accretion on various surfaces [27–30], some other researchers suggested that super-hydrophobic surfaces with nano/micro textures do not necessarily imply icephobicity [31], especially under dynamic water impacting conditions in which the transition from the Cassie-Baster state to the Wenzel state is more readily to occur [32]. In order to examine the performance of the novel *n*HSN-treated surfaces in terms of water-/ice-repellency, a series of experiments were performed in the present study to not only characterize the surface structures and wettability of the *n*HSN-treated surfaces, but also evaluate the effects of the *n*HSN treatment on the dynamic droplet impacting processes as well as their capability in reducing ice adhesion strength.

In the context that follows, a detailed description of the operational procedures of the *n*HSN treatment on AA-6061 aluminum alloy samples will be introduced at first. Then, a series of experiments will be performed to characterize the *n*HSN-treated surfaces in terms of surface wettability and icephobicity, i.e., more specifically, contact angles of water droplets in static and dynamic conditions, impacting dynamics of water droplet, and ice adhesion strength, in comparison with the surfaces of an untreated bare aluminum plate sample and a only laser-texted aluminum plate sample.

2. Surface treatment with *n*HSN technique

In the present study, a novel *n*HSN method is introduced to manufacture super-hydrophobic surfaces on AA-6061 aluminum samples. This novel process consists of two steps: (1) water-confined nanosecond laser texturing, during which a high energy nanosecond-pulse-laser scans the material surface contained under water using a large spatial increment and a fast processing speed; (2) chemical immersion treatment, during which the laser textured surface is further chemically treated.

2.1. Water confined nanosecond laser texturing (wNLT)

The water confined nanosecond laser texturing was achieved by using a high-energy Q-Switch Nd:YAG nanosecond laser (Spectra-Physics Quanta-Ray Lab-150, wavelength 1064 nm), which can generate pulsed laser with energy on the order of several hundreds of mJ/pulse. During the laser texturing process, the laser repetition rate was set to be 10 pulses per second with a laser pulse duration of 6–8 ns. A galvanometer laser scanner (SCANLAB intelliSCAN® 20) furnished with an f-theta objective with a focal length of 255 mm was utilized to direct the laser to texture the top surface of the specimen. The specimen was submerged in deionized water, which confined the laser pulse-induced plasma and enhanced the texturing effect. Due to the effect of confinement water medium during laser texturing with nanosecond pulsed laser, the expansion of plasma was confined. At the same time, the water medium confined the ejected hot mass during laser scanning, leading to a more violent laser-material interaction and higher possibility of phase explosion [33]. In addition, water confinement added peening effect to the textured surface to increase the hardness [26]. The static water contact angle of laser textured samples processed with 2.4GW/cm^2 laser power intensity was compared for both with water and without water confinement and both of them underwent chemical treatment after laser texturing. The static contact angles were found to be 167.1° ± 1.2° and 126.7° ± 2.1° respectively for the test cases with and without water confinements. This shows that water confinement helped to increase the texturing effect.

Fig. 1 shows the schematic of the water-confined nanosecond laser texturing system. The workpiece was kept in deionized water confinement (around 8 mm depth from the specimen surface) in a tank, which was positioned using computer-controlled stages. The laser scan head scans the top surface of the specimen in a zig-zag pattern. The X-spacing (or pitch) defines the distance between two sequential laser scan lines and is pre-set through computer control. The Y-spacing between two sequential laser shots along the scanning direction is determined by the Laser Repetition Rate and pre-set Laser Scanning Speed. The Overlap Ratio is set by the ratio of Overlap Area to the Laser Spot Area. For all the samples prepared in this study, a same value was applied for both X-spacing and Y-spacing, which guarantees the same Overlap Ratio of 50% in both directions. The Laser Spot Area can be adjusted by moving the Z stage away from the focal plane.

The combination of laser scan head and computer-controlled stages allows for a wider range of laser scanning area during the treatment.

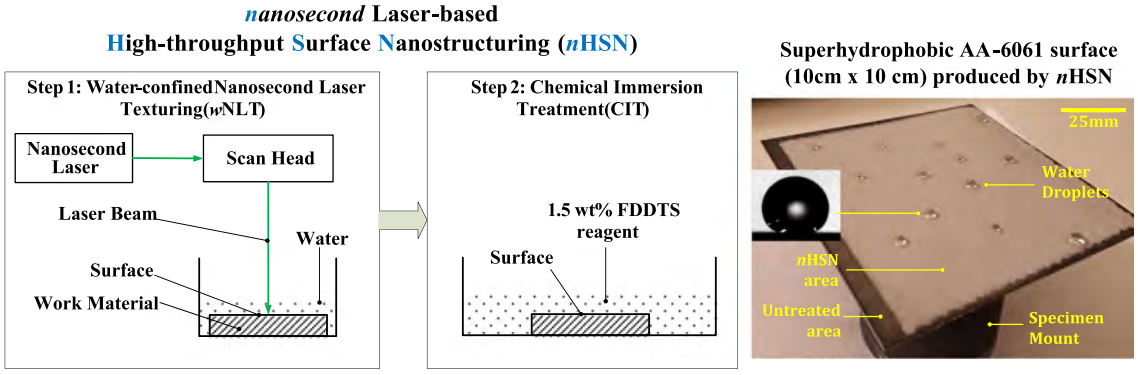

Fig. 1. Schematic of the *n*HSN approach and the processed AA-6061 sample with water droplets sitting on the surface.

Both laser and scan heads were controlled by a microcontroller for scanning along a pre-designed path. The scan head was also connected to a water cooling system to avoid any undesirable overheating of the scan head during the texturing process.

2.2. Chemical immersion treatment (CIT)

After the laser texturing, the workpiece was immersed in an ethanol solution with 1.5% volume percentage chlorosilane reagent [$CF_3(CF_2)_9CH_2CH_2SiCl_3$], also known as FDDTS at room temperature for ~3 h as shown in Fig. 1. The workpiece was then cleaned with deionized water and dried using compressed air. Finally, it was kept at 80 °C in a vacuum oven for 1 h to dry it out completely. After that, the specimen was checked for superhydrophobicity by sprinkling water droplet on the processed surface as shown in Fig. 1.

Fig. 2 shows the SEM images of the untreated bare AA-6061 aluminum surface, *w*NLT-treated and the *n*HSN-treated surfaces for comparison. It is clearly seen that the surface morphology of the AA-6061 sample is significantly changed after the *w*NLT and *n*HSN treatment. While the surface of the untreated AA-6061 aluminum appears to be smooth and uniform with some intrinsic textures and minor defects, the *w*NLT-treated surface is found to become highly disordered with a great deal of bulges and concaves. Randomly distributed microscale ripples can be observed, and on top of those ripples, nanoscale protrusions, and particles with a size of a few hundreds of nanometers can be observed. After the CIT process, the disordered surface is maintained, and nanoscale particles still exist on top of the ripples. These micro/nano hierarchical structures are suggested to be the contributing features that promote the superhydrophobicity of the *n*HSN-treated surfaces. At the same time, the surface chemistry modified by FDDTS reagent also contributed towards the superhydrophobicity.

For the throughput analysis of different laser-based surface texturing methods, the main parameter to be discussed is Specific Laser Scanning Time (SLST), i.e., the time needed to treat a unit area of 1 in^2. A shorter SLST would indicate a higher efficiency in the surface treatment, thereby a higher process throughput. Fig. 3 compares the SLST of the *n*HSN approach and other existing laser-based surface texturing methods. For *n*HSN using the Spectra-Physics Quanta-Ray Lab-15 ns laser, a Specific Laser Scanning Time of 7.2 s/in^2 (or 0.12 min/in^2) can be achieved by using the following process parameters: Laser Power Intensity of 0.20 GW/cm^2, Pulse Energy of 710 mJ, Laser Spot Diameter of 7.5 mm, Y-spacing of 3 mm, Laser Scan Line Density of 4 lines/in,

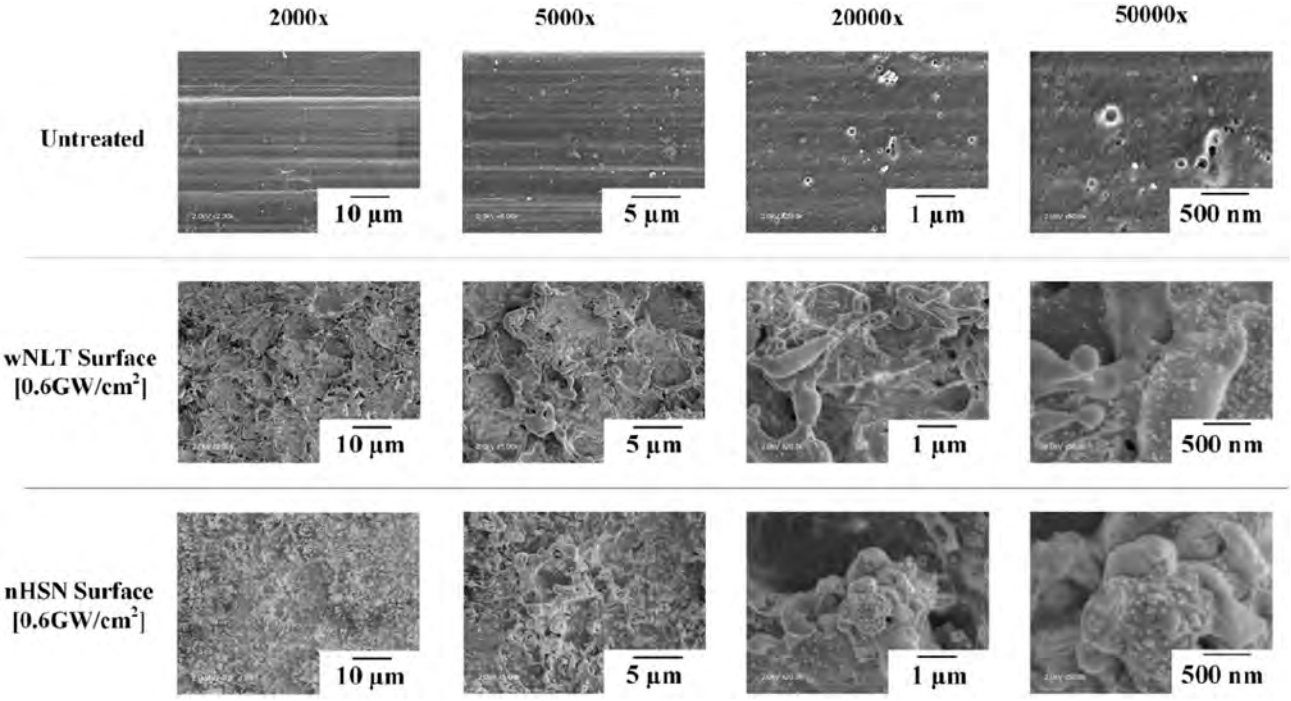

Fig. 2. SEM images of the untreated, *w*NLT and *n*HSN treated AA-6061 aluminum surfaces. The *w*NLT and *n*HSN processes are carried out with laser power intensity 0.6GW/cm^2.

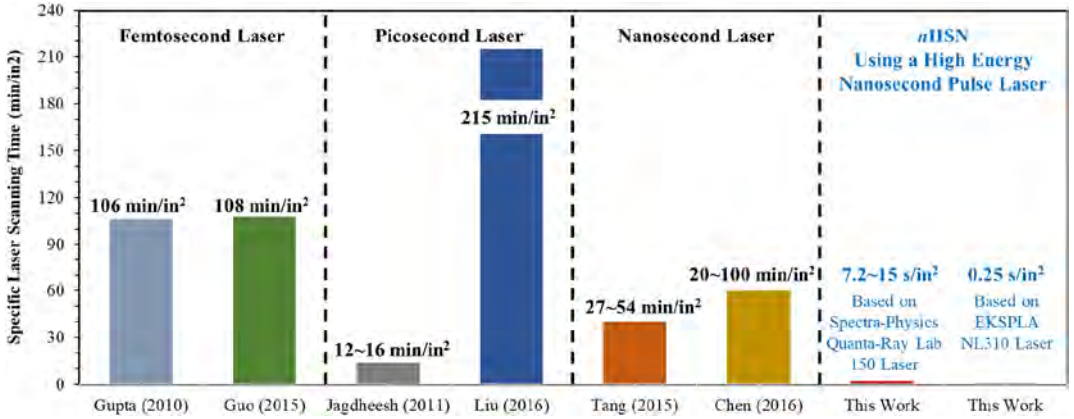

Fig. 3. Specific Laser Scanning Time using *n*HSN and other existing laser-based surface texturing methods.

Overlap Ratio of 50%, Laser Repetition Rate of 10 pulses per second, and Laser Scanning Speed of 30 mm/s. An industry-level nanosecond laser will further scale up the Laser Processing Rate and enable a larger area by using a higher Pulse Energy and a higher Laser Repetition Rate, while maintaining the same Laser Power Intensity. For example, by using the EKSPLA NL310 series Q-switch Nd:YAG Laser, the SLST of *n*HSN can be significantly improved to 0.25 s/in^2 (or 0.004 min/in^2) following these process parameters: Laser Power Intensity of 0.20 GW/cm^2, Pulse Energy of 10 J, Laser Spot Diameter of 4 cm, Y-spacing of 1.6 cm, Overlap Ratio of 50%, Laser Repetition Rate of 20 pulses per second, and Laser Scanning Speed of 160 mm/s. For femtosecond laser surface texturing, the data of typical SLST is obtained from patents US 2010/0143744 A1 [34], US 2015/0136226 [35], research papers by Steele et al. [36] and Vorobyev and Guo [14]. For picosecond laser surface texturing, the data of typical SLST is obtained from research papers by Jagdheesh et al. [37] and Liu et al. [38]. For nanosecond laser surface texturing, the data of typical SLST is obtained from research papers by Tang et al. [21] and Chen et al. [20]. It is clearly seen that, in comparison with the existing ultrashort laser-based surface texturing techniques, the *n*HSN process significantly increases the processing rate from hundreds of minutes per square inch to seconds, and also enables larger area processing for practical throughput.

In the present study, five different surfaces were prepared for the comparative study as listed in Table 1. While a bare aluminum AA 6061 sample (i.e., Sample #1) is prepared as the baseline surface, a laser-textured surface without any chemical treatment (i.e., Sample #2) is also prepared as a reference sample to examine the effects of chemical treatment on the surface characteristics. Since the laser power intensity could essentially affect the depth of the surface textures during the laser treatment, thereby affect the surface characteristics, three *n*HSN surfaces treated with different laser power intensity levels (i.e., 0.6 GW/cm^2, 2.4 GW/cm^2, and 8.4 GW/cm^2) were prepared to evaluate the effects of laser power intensity on the resulting surface characteristics, e.g., surface wettability and ice adhesion strength. As a reference, Fig. 4 shows the micro/nanoscale surface features generated under the different laser power intensity conditions. It is clearly seen that, the density of the nanoscale structures is higher in case specimen processed with higher laser intensity. The feature size is also reduced as the laser power intensity is increased.

Table 1
Test samples in the present study.

Sample #	Substrate material	Laser power density	CIT process
1	AA 6061	0 GW/cm^2	No
2	AA 6061	8.4 GW/cm^2	No
3	AA 6061	8.4 GW/cm^2	Yes
4	AA 6061	2.4 GW/cm^2	Yes
5	AA 6061	0.6 GW/cm^2	Yes

3. Experimental setup to characterize the *n*HSN-treated surfaces

3.1. Experimental setup used to measure the static and dynamic contact angles on the nHSN-treated surfaces

To characterize the wettability of the *n*HSN-treated surfaces, both static and dynamic (i.e., advancing and receding) contact angles of water droplets on the test surfaces were experimentally measured. The schematic of the experimental setup for the contact angle measurements is depicted in Fig. 5. A high-speed imaging system (PCO Tech, Dimax) using a high-magnification 12× zoom lens system (LaVision) was positioned with a view from the side of the 50 mm × 50 mm substrate mounted on a vertical translation stage. A droplet generation system, i.e., which includes a syringe pump (GenieTouch™ Syringe Pump, Kent Scientific) used to precisely control the droplet size and a syringe used to generate deionized water droplet through a needle, was mounted above the test substrate. A 20 W LED lamp (i.e., Dot Line RPS Studio, RS-5410) illuminating a piece of frosted glass was used to provide back-illumination for the droplet imaging. During the measurements, a synchronizer (Berkeley Nucleonics, model 575) along with an oscilloscope (Tektronix DPO3054) was used to control the image acquisition rate of the high-speed imaging system.

In the present study, while the static contact angle, i.e., θ_{static}, of water droplet was measured by digitizing the images of sessile deionized water droplet over the test surfaces, the dynamic contact angles (i.e., advancing, θ_{adv}, and receding, θ_{rec}) were measured by digitizing the transient images of water droplets during the expanding and contracting processes (i.e., each substrate was tested by forcing water through the needle using the syringe, thereby creating an expanding droplet with an advancing contact line; then, the syringe was used to pull the water back into the needle, causing the droplet to shrink and the contact line to recede). The hysteresis $\Delta\theta$ is defined as the difference between θ_{adv} and θ_{rec}. It should be noted that the measurements of static and dynamic contact angles were performed under the same test conditions, in which the ambient temperature was set at 20 °C, and the relative humidity was 50%.

The images recorded with the high-speed imaging system were analyzed using a custom MATLAB code. The time sequence of the droplet images were imported into MATLAB, where for each image, a line-detector was implemented to identify the pixels on substrate surface and the droplet edges. Then, linear and quadratic best-fit curves were computed for the substrate surface and the droplet edge, respectively, using a least squares fitting to the corresponding edge pixels. The intersection of the two fitting curves denotes the contact line location, while the relative angle between the lines at their intersection determines the contact angle.

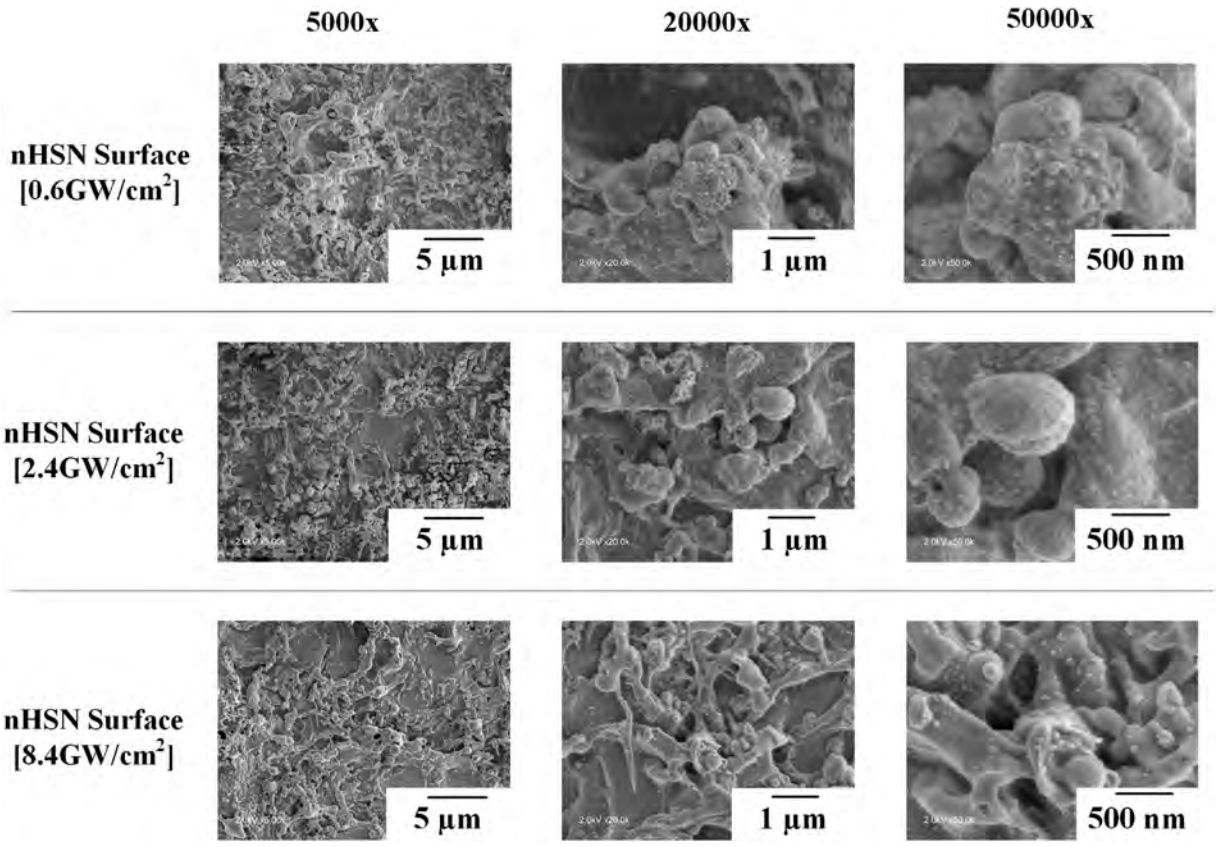

Fig. 4. Comparison of surface morphology of nHSN treated AA6061 surface with different laser power intensity.

3.2. Experimental setup used to study the dynamic droplet impacting processes on the nHSN-treated surfaces

Since most of the water corrosion and ice accretion events observed on the various engineering structures are found to occur along with dynamic water droplet impingement, a better knowledge of the fundamental mechanisms of dynamic droplet impingement on different surfaces (i.e., hydrophilic vs. superhydrophobic) is of great importance in elucidating the effects of surface wettability on the ice accretion process. In the present study, the impinging dynamics of water droplets onto the different test surfaces were experimentally investigated to provide more details of the fundamental mechanisms in droplet-surface interactions during the dynamic droplet impinging processes over the different surfaces.

Fig. 6 shows the schematic of the experimental setup used in the present study to characterize the dynamic impacting processes of water droplets onto the different test surfaces. During the experiments, a trigger system was used to generate a pulse signal when a water droplet passing through the laser light. The pulse signal was then sent to a high-speeding imaging system (Fastcam Mini WX100, Photron, with a macro-lens, 50 mm Nikkor 1.8D, Nikon), which was used to record the transient details during the dynamic droplet impinging processes. To provide high-quality images of the impacting droplets, a LED spotlight was used to illuminate the droplet impacting on the test surfaces. For each test case, the image acquisition rate was set at 5000 Hz, so that the dynamics (i.e., droplet spreading, receding, and rebounding) of the impacted droplet can be well resolved.

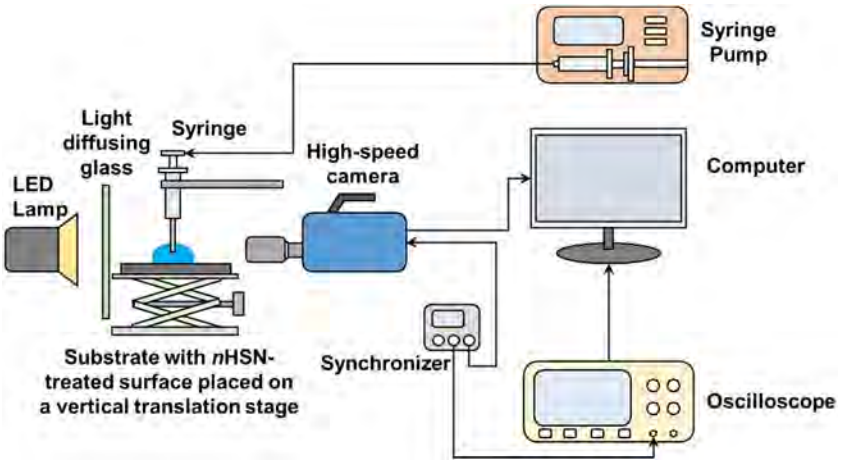

Fig. 5. Experimental setup to study the surface wettability of the *n*HSN-treated surfaces.

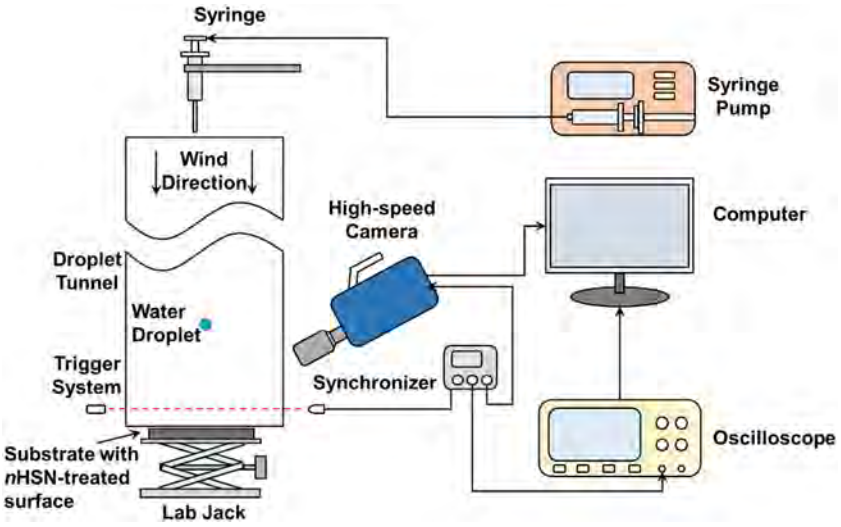

Fig. 6. Experimental setup to study the dynamic droplet impacting process over the *n*HSN-treated surfaces.

3.3. Experimental setup used to measure ice adhesion strength of the nHSN-treated surfaces

In the present study, the ice adhesion strengths over the *n*HSN-treated surfaces were also measured by using a push-to-shear mechanism, as suggested by Meuler et al. [31]. Fig. 7 shows the schematic of the experimental setup used in the ice adhesion strength measurements of the different test surfaces. The experimental setup consists of an environmental chamber housing a digitally controlled Peltier cooler (TETech CP061 and TC-48-20) and a linear actuator with integrated motion controller (Newport CONEX-LTA-HS) that drives a 40 N range force-torque transducer (JR3 30E12A4) supporting an aluminum force probe. The force signals were recorded by a 16-bit data acquisition card (NI PCI-6052E). A 3D-printed ice mold is used to create a 8 mm diameter ice cylinder on the test substrate, which is a 50 mm × 50 mm sample placed on the Peltier cooler.

The diagram of the ice adhesion measurement is also illustrated in Fig. 7, which identifies the diameter of the ice cylinder, D, the mold shell thickness, t, the height of the displacement probe, h, and the probe contact face height, δ. With the test sample being firmly attached on the Peltier cooler, the surface temperature of the test sample can be well maintained below the freezing point. During the experiments, the Peltier cooler was first turned on and set to the test temperature (e.g., −10 °C in the present study). After about 30 min, allowing for the stabilization of surface temperature, the ice mold was placed onto the surface of the freezing cold test sample. Then, a syringe was used to slowly inject deionized water into the mold to produce ice cylinder adhered to the test surface. It should be noted that, in order to keep the injected water secured in the ice mold with no water leakage or bubble formation during the freezing process, the ice mold bottom was treated to be superhydrophobic to keep the gap between the mold and the test surface being free of water/ice. In the present study, a low-temperature environmental chamber (i.e., filled with carbon dioxide released from sublimating dry ice) was also used to provide a humid-air free environment (i.e., no condensation over the test surface) for the ice adhesion measurements. After the freezing process was completed, the force probe was aligned with the sample and set at 0.5 mm above the test surface. A custom MATLAB code was used to sample the voltage signals from the force transducer at 2000 Samples/s. For each test case, a tare measurement was performed for 10 s prior to bringing the probe into contact with the ice sample. The ice adhesion force data was recorded while the linear actuator stage was moved at a rate of about 0.5 mm/s until the ice was sheared off the surface.

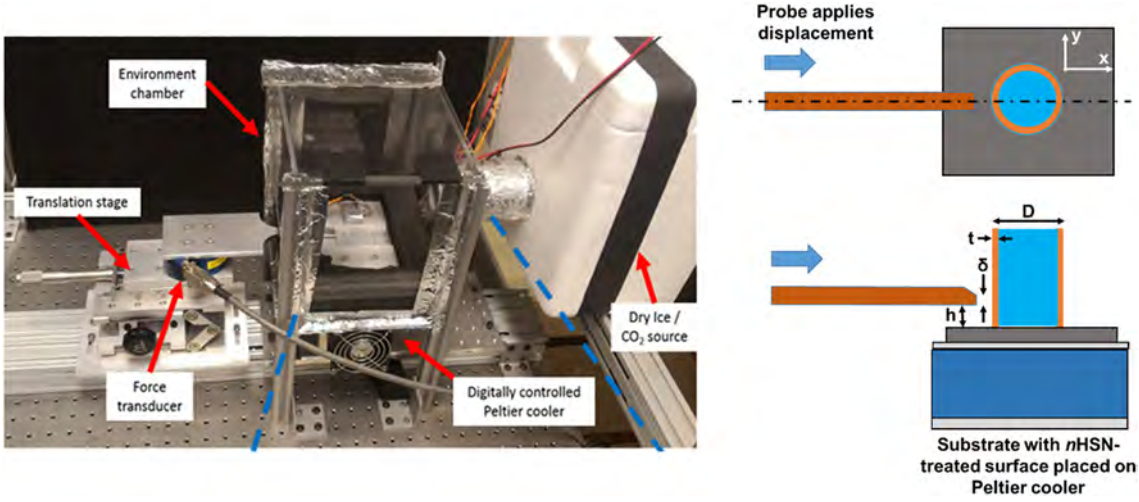

Fig. 7. Experimental setup to measure the ice adhesion strength over the *n*HSN-treated surfaces.

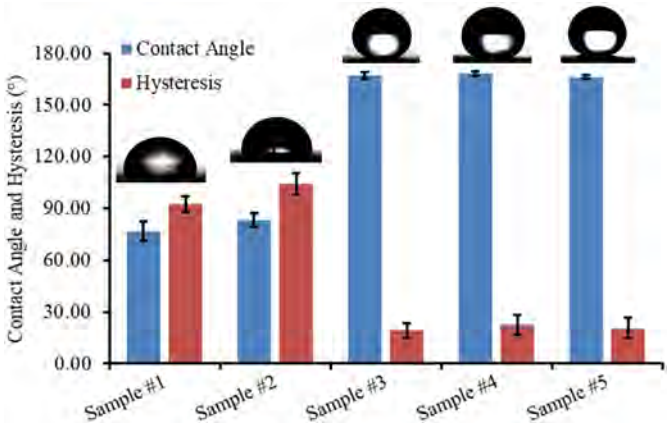

Fig. 8. Measured contact angle and hysteresis of water droplets sitting on the different surfaces.

4. Measurement results and discussions

4.1. Wettability of the nHSN-treated surfaces

Wettability describes how a liquid interacts with a solid surface. For a droplet sitting on a surface, a three-phase system is formed: the liquid droplet, the solid surface contacting with the droplet, and the gas surrounds the droplet. The shape of the droplet is essentially determined by the liquid-solid, liquid-gas, and solid-gas interaction energies [39]. In order to characterize the wettability of the *n*HSN-treated surfaces, a series of experiments were conducted in the present study to not only measure the static contact angles, i.e., θ_{static}, of water droplets sitting on the different surfaces listed in Table 1, but also quantify the dynamic contact angles (i.e., advancing, θ_{adv}, and receding, θ_{rec}) of water droplets during the expanding and contracting processes over the different surfaces.

Fig. 8 shows the images of water droplets sitting on the different surfaces as well as the static contact angles measured by digitizing the droplet images [40,41]. It is clearly seen that, though the static contact angle of water droplet on the only laser-textured surface (i.e., Sample #2) is increased in comparison to that on the untreated bare AA-6061 aluminum sample (i.e., Sample #1), i.e., $\theta_{static} = 76^{\circ}$ for Sample #1 and $\theta_{static} = 83^{\circ}$ for Sample #2, both of them are smaller than 90°, indicating that the surfaces of the two samples are hydrophilic. It is worth mentioning that, the contact angle of the laser textured surface without deposition of FDDTS, i.e., Sample #2, was not measured immediately after the laser texturing. It was measured after 7 days of laser texturing. The contact angle measured immediately after laser texturing was found to be only about 11°. The increased contact angle of droplet over the surface of Sample #2 after a period of exposure to air is suggested to be caused by the contamination of the rough surface by the airborne organics [42].

The measured static contact angles of water droplets on the *n*HSN-treated surfaces (i.e., Sample #3, #4, and #5) were found to be almost the same, i.e., $\theta_{static} \approx 167^{\circ}$, which is similar to those of the measured values of the laser treated surfaces reported recently by other research groups [42–45]. Table 2 gives a comparison of the surface wettability obtained with different laser treatments. It is clearly seen that, while the laser spot diameter and scanning pitch are set to be much larger in the present study (i.e., resulting in a much faster speed in the laser treatment, in comparison to the laser-treated surfaces of the previous studies [42–45]), the *n*HSN-treated surfaces appear to have evident superhydrophobicity. While the *n*HSN-treated surfaces are superhydrophobic, their wettability is almost not dependent on the laser power intensity. Again, the θ_{static} was monitored for a period of 30 days with two measurements each day. During this period, the samples were kept in open air without long-term contact with water. There was no decrease of the θ_{static} over this period with a variation of ± 1.5°. It should also be noted that the static contact angle of a non-textured sample with only CIT process was also measured, which is 93° ± 1.3°. It demonstrates that, though the CIT process could increase the hydrophobicity of the non-textured sample surface, it is not very effective in comparison to the two-step *n*HSN methods (laser treatment + CIT process).

In the present study, the dynamic contact angles (i.e., advancing, θ_{adv}, and receding, θ_{rec}) of water droplets over the different test surfaces were also measured during the expanding and contracting processes. While the droplet shapes formed on the untreated bare AA-6061 aluminum surface are significantly different during the expanding and contracting processes (i.e., the contact angle of droplet is about $\theta_{adv} = 104^{\circ}$ when the contact line is advancing vs. the contact angle is only about $\theta_{rec} = 10^{\circ}$ when the contact line is receding), the droplet shape formed on the *n*HSN-treated surface is only slightly changed during the expanding and contracting processes (i.e., the contact angle of droplet is about $\theta_{adv} = 172^{\circ}$ when the contact line is advancing vs. the contact angle is about $\theta_{rec} = 153^{\circ}$ when the contact line is receding). It is suggested that the different droplet morphologies formed during the advancing and receding processes are essentially due to the facts that the moving droplets are in energetically metastable states, in which the droplets are prevented from reaching the minimum-energy state [39]. Based on the measured advancing and receding contact angles of water droplets on the different surfaces, the contact angle hysteresis (i.e., $\Delta\theta = \theta_{adv} - \theta_{rec}$) is also calculated, and plotted in Fig. 8. It is found that while the contact angle hysteresis of droplets on the untreated bare aluminum surface and the laser-textured surface without chemical treatment are larger than 90°, the contact angle hysteresis of droplets on the *n*HSN-treated surfaces are much smaller, i.e., $\Delta\theta \approx 20^{\circ}$.

As reported by Waldman et al. [46] and Liu et al. [3,47], for a water droplet deposited on a surface, the capillary force can be calculated using the following equation:

$$F_{capillary} \approx \pi R \gamma_{LG} \left[\sin\left(\frac{\theta_{adv} - \theta_{rec}}{2}\right) \sin\left(\frac{\theta_{adv} + \theta_{rec}}{2}\right) \right] \quad (1)$$

where R is the spherical cap radius of the water droplet moving over a surface, and γ_{LG} is the liquid-gas surface tension. When an external force is applied onto the droplet, which overcomes the capillary force that resists the water droplet to move, the droplet would be in motion. For the water droplets with the same spherical cap radius moving on different surfaces (untreated bare aluminum surface vs. *n*HSN-treated surface), the ratio of the capillary forces can be calculated based on the receding and advancing contact angles measured above:

$$\frac{F_{cap,nHSN}}{F_{cap,baseline}} \approx \frac{\left[\sin\left(\frac{\theta_{adv}-\theta_{rec}}{2}\right)\sin\left(\frac{\theta_{adv}+\theta_{rec}}{2}\right)\right]_{nHSN}}{\left[\sin\left(\frac{\theta_{adv}-\theta_{rec}}{2}\right)\sin\left(\frac{\theta_{adv}+\theta_{rec}}{2}\right)\right]_{baseline}} \approx 0.08 \quad (2)$$

It is found that the capillary force acting on the water droplet over the *n*HSN-treated surface is much smaller (i.e., becoming only about 8%) in comparison with that acting on the water droplet with the same spherical cap radius siting on the untreated bare aluminum surface. Thus, the external force required to move water droplets over the *n*HSN-treated surface is much smaller (i.e., being only ~ 8% in magnitude), in comparison with those on the untreated bare aluminum surface. The water droplets deposited on the *n*HSN surfaces are expected to be much easier to be removed by an external force, e.g., gravity or aerodynamic drag force.

4.2. Dynamic impinging process of water droplets onto the nHSN-treated surfaces

In the present study, the impinging dynamics of water droplets onto the different test surfaces (i.e., the untreated bare aluminum surface, Sample #1, the laser-textured aluminum surface without chemical

Table 2
Comparison of surface wettability obtained with different laser treatments.

Substrate material	Laser spot diameter (μm)	Laser scanning rate (mm/s)	Scanning pitch (μm)	Laser power intensity (GW/cm^2)	WCA (°)	Data source
Al6061	90	2000	4	0.25	70	Rico et al. [42]
Al6061	90	2000	20	0.25	140	Rico et al. [42]
Al6061	90	100	20	0.25	155	Rico et al. [42]
Al-Mg	40	50	20	380	171.8	Boinovich et al. [43]
Al6061	7.5×10^3	30	8.5×10^3	0.6	167.3	Present study
Al6061	7.5×10^3	30	8.5×10^3	2.4	168.0	Present study
Al6061	7.5×10^3	30	8.5×10^3	8.4	166.3	Present study

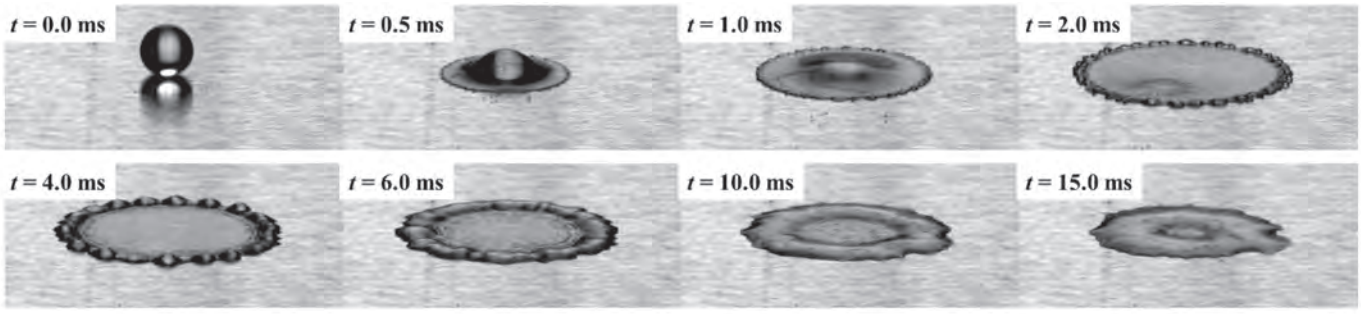

(a). Dynamic impingement of a water droplet onto the untreated bare aluminum surface (i.e., Sample #1)

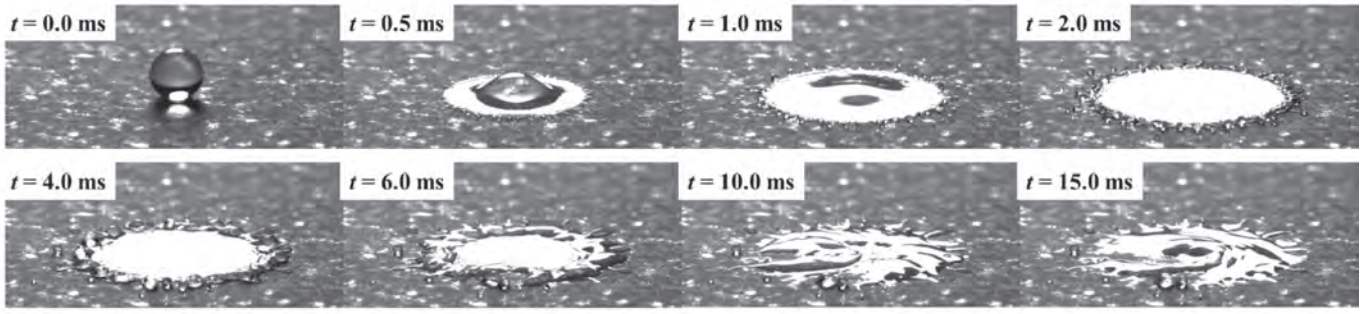

(b). Dynamic impingement of a water droplet onto the only laser-treated surface (i.e., Sample #2)

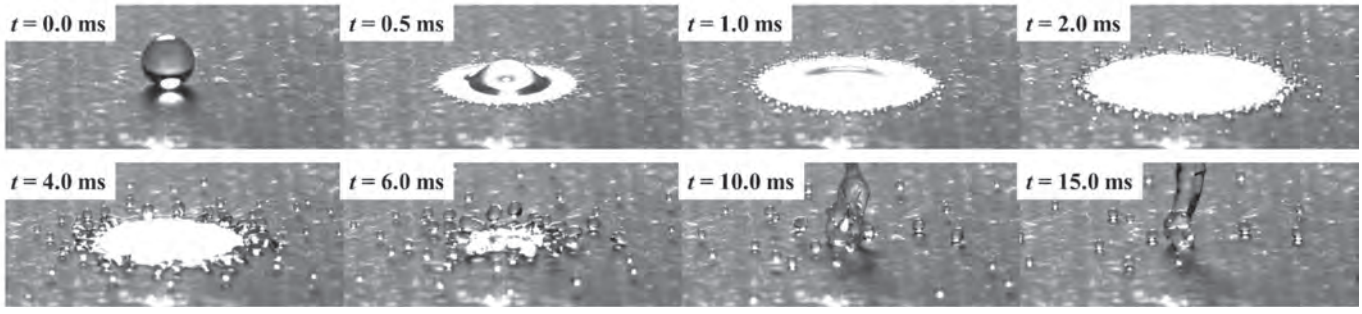

(c). Dynamic impingement of a water droplet onto the *n*HSN-treated surface (i.e., Sample #3)

Fig. 9. Time-evolutions of the dynamic impinging processes of water droplets onto the different test surfaces at the Weber number of $We \approx 300$.

treatment, Sample #2, and the *n*HSN-treated aluminum surface, Sample #3) were also experimentally investigated to provide the very important transient details of the droplet-surface interactions during the dynamic water droplet impacting processes on the different surfaces.

Fig. 9 shows typical snapshot images to reveal the dynamics of water droplet impinging onto the different test surfaces at the Webber number of about 300 (i.e., $We \approx 300$), which is defined as $We = \rho V^2 D/\sigma$, where ρ is the density of a droplet (kg/m^3); V is the velocity of the droplet (m/s); D is the droplet diameter (m); and σ is the surface tension (N/m). As shown clearly in Fig. 9(a), when the water droplet impacted onto the untreated bare aluminum surface (i.e., Sample #1), the impinged water mass was found to spread out rapidly over the rigid surface. During the spreading process, tiny substructures, i.e., water beads, were found to be formed along the rim of the out-spreading ring of the impinged waster mass as can be seen clearly from $t = 1.0$ ms to $t = 4.0$ ms. As suggested by Xu et al. [48], there are two stresses contributing to the dynamics of the spreading droplet: one is due to the restraining pressure of the gas on the spreading liquid, which acts to

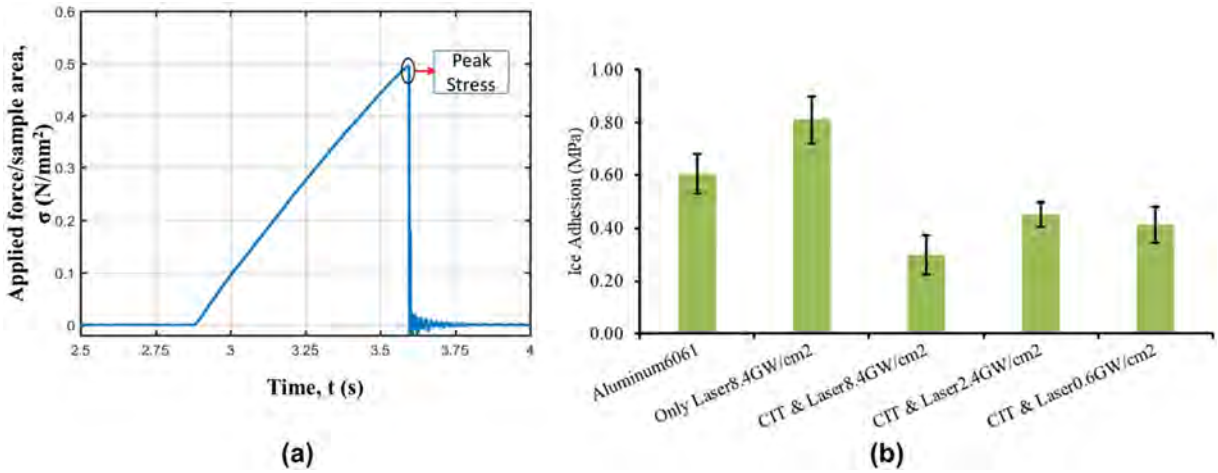

Fig. 10. (a) Time-history of the measured force-per-area data for the untreated aluminum 6061 sample; (b) measured ice adhesion strength over the different test surfaces.

destabilize the advancing front and deflect it upward; the other is due to the surface tension of the liquid, which favors keeping the liquid layer intact after impact. As the two stresses become comparable, the expanding water rim would be destabilized, i.e., with the formation of the "bead-like" substructures as shown in Fig. 9(a) or the ejection of droplets at higher Webber numbers [49]. After reaching its maximum spreading diameter, the impinged water mass was found to recede with the surface water being collected to the impinging center. As the water mass receded, i.e., $t = 6.0$ ms to $t = 15.0$ ms, the previously formed water beads were found to be "relaxed" and merged into a smooth ring as shown in Fig. 9(a). Finally, the impinged water mass reached the static state and settled down in a formation of water film over the surface. During the entire spreading and receding process of the impinged droplet on the untreated bare aluminum surface, there was almost no water mass being splashed out from the main droplet body.

The time-evolution of the dynamic water droplet impinging process on the laser-textured surface without chemical treatment (i.e., Sample #2) is shown in Fig. 9(b). Though the aluminum surface structures were significantly changed by applying the laser texturing, the droplet impinging behavior on this surface was found to be very similar to that on the untreated surface (i.e., Sample #1). While the water mass was rapidly spread out upon impacting on the surface, the rim of the outspreading ring of the impinged waster mass was found to break into tiny substructures, i.e., formation of the tiny water beads along the rim from $t = 1.0$ ms to $t = 2.0$ ms. It should be noted that, during the spreading process, while most of the substructures along the rim were kept attaching to the main droplet body, a small amount of water mass was found to be splashed out, forming the satellite water droplets, as can be seen in the snapshots at $t = 2.0$ ms to $t = 4.0$ ms. After reaching its maximum diameter, the impinged water droplet was found to recede with the water mass flowing back to the impinging center. Due to the anisotropy of the highly textured surface, the receding water mass was found to be in a very different morphology in comparison to that on the surface of Sample #1, i.e., while a relatively smooth ring of water was formed at the beginning of the receding process ($t = 6.0$ ms), the receding ring broke up thereafter with the water mass being distributed nonaxisymmetrically as can be seen in the snapshots at $t = 10.0$ ms to $t = 15.0$ ms in Fig. 9(b).

For the droplet impinging (at the same Webber number, i.e., $We \approx 300$) onto the *n*HSN-treated surface, it was found that, while the impinged water mass underwent a similar spreading process as that over the surfaces of Sample #1 and Sample #2, both receding (see instants from $t = 2.0$ ms to $t = 4.0$ ms) and rebounding (see instants from 6.0 ms to 15.0 ms) processes were observed after the corona splashing as shown in Fig. 9(c). In comparison to the surfaces of Sample #1 and Sample #2, the *n*HSN-treated surface has been demonstrated to be superhydrophobic with a much larger static contact angle ($\theta_{static} < 90^\circ$ for Sample #1 and Sample #2 vs. $\theta_{static} = 167^\circ$ for the *n*HSN-treated surface) and a much smaller contact angle hysteresis ($\Delta\theta > 90^\circ$ for Sample #1 and Sample #2 vs. $\Delta\theta \approx 20^\circ$ for the *n*HSN-treated surface). The impinged water mass on the *n*HSN-treated surface would only contact and move over the tips of the rough surface with air pockets trapped underneath the water droplet [50]. Thus, the capillary force of the water droplet on the *n*HSN-treated surface was much smaller in comparison with that on the surfaces of Sample #1 and Sample #2 (i.e., only about 8% in magnitude). The receding velocity of the impinged water mass, therefore, was much larger due to the very small capillary force to resist the surface water movement. As a result, the inertia energy of the receding water droplet was almost kept not changed, leading to the upward rebounding of the water mass on the *n*HSN-treated surface. It should be noted that, much more "satellite" droplets were found to be formed during the splashing and receding processes of the impinged water droplet on the *n*HSN-treated surface.

4.3. Ice adhesion strength of the nHSN-treated surfaces

In the present study, the ice adhesion strengths of the different test surfaces were also measured quantitatively by using the experimental setup shown in Fig. 7. During the experiments, the temperature of the test surface was maintained at a pre-scribed low temperature (i.e., at $T_w = -10^\circ$ for the present study). Since the force values for time step were easily discernable in the data, a force vs displacement relationship was acquired from the known probe speed and time taken for the interface failure as shown in Fig. 10(a). The applied force was calculated by multiplying the transducer's calibration matrix to the voltage signals of the force transducer. Thus, the average shear force per adhesion area was derived by dividing the applied force by the contact area of the ice sample. The adhesion strength was taken as the maximum force-per-area observed before failure. Ten test trials were performed for each test case, and the mean and standard deviation values of the ice adhesion strength were obtained based on the measurement results.

Fig. 10(b) shows the ice adhesion strength of the different test surfaces. The measurements were conducted with the temperature of the test surfaces being kept at $T_w = -10\,^\circ$C. It is found that the ice adhesion strength of the untreated bare aluminum AA-6061 surface (i.e., Sample #1) is about 0.60 MPa, which agrees well with the data available in literatures [51]. For the laser-textured surface without any chemical treatment (i.e., Sample #2), the ice adhesion strength is increased to about 0.80 MPa. Since the surface is still hydrophilic after the laser texturing, the overall contact area of droplet on the surface of

Sample #2 is almost the same with that on the surface of Sample #1. However, due to the existence of the micro/nano textures over the surface, ice structures would penetrate into the surface textures, so that the effective contact area of the ice sample is actually increased with "ice anchors" locked in the surface textures, resulting in the increase of ice adhesion strength. For the laser-textured surfaces with chemical treatment (i.e., *n*HSN-treated surfaces, Sample #3, #4, and #5), the ice adhesion strength is found to be significantly reduced (i.e., about 0.30–0.40 MPa). As suggested by Kulinich and Farzaneh [52], the ice adhesion strength on rough hydrophobic surfaces is correlated well with the wetting hysteresis, which is believed to be related to the ice-solid contact area. Thus, the lower ice adhesion strengths of the *n*HSN-treated surfaces are essentially caused by the smaller ice-surface contact area during the freezing process. It should be noted that, while the *n*HSN-treated surfaces are characterized with similar contact angles, the ice adhesion strength of them appears to be scattered, which is suggested to be caused by the variation of void content at the ice-solid interface that is closely related to the variation of micro/nano feature scales generated under the different laser intensity conditions. While the *n*HSN-treated surfaces exhibit evident superhydrophobicity and reduced ice adhesion, their durability under consistent water/ice contact conditions is still a big concern [53], which needs to be addressed in the futures.

5. Conclusion

In the present study, an experimental study was performed to characterize the laser-textured surfaces fabricated by using the novel *n*HSN method. Based on the throughput analysis of different laser-based surface texturing methods in the term of Specific Laser Scanning Time (SLST), it is found that the *n*HSN process significantly increases the processing rate from hundreds of minutes per square inch to seconds in comparison to the existing ultrashort laser-based surface texturing techniques.

A series of experiments were performed to examine the performance of the *n*HSN surfaces in the term of "water/ice-repellency". It is found that, while the untreated aluminum surface and the laser-textured aluminum surface are hydrophilic with the static contact angle being smaller than 90°, the *n*HSN-treated surfaces appear to be superhydrophobic with a much larger static contact angle (i.e., ~170°) and a much smaller contact angle hysteresis (i.e., ~20°). Due to the significantly increased contact angle and reduced hysteresis of water droplet on the *n*HSN-treated surfaces, the capillary force acting on the water droplet sitting over the *n*HSN-treated surface was found to be much smaller (i.e., becoming only about 8% of that over the untreated bare aluminum surface). Therefore, the water droplets deposited on the *n*HSN-treated surfaces would be much easier to be removed by an external force with a magnitude of only ~ 8% of those on the untreated aluminum surface.

By comparing the dynamic water droplet impacting processes over different test surfaces, it was found that, while the impinged water mass undergoes a similar spreading process over the different test surfaces (i.e., untreated aluminum surface, laser-textured surface, and *n*HSN-treated surface), the receding processes of the impinged water droplet on the different surfaces appear to be very different. The impinged water mass was found to be rebounded much more rapidly on the *n*HSN-treated surface, leading to the upward ejection of the impacted water mass as it recedes with a much larger velocity, which is essentially due to the much higher inertia energy of the receding water mass over the *n*HSN-treated surface. Much more "satellite" droplets are also found to form during the splashing and receding processes of the impinged water droplet on the *n*HSN-treated surface. The superhydrophobicity of the *n*HSN-treated surfaces is further promoted to "ice-repellency" by the reduced ice adhesion strength, which is believed to be caused by the much smaller ice-solid contact area on the *n*HSN-treated surface.

Acknowledgements

The research work is partially supported by National Aeronautics and Space Administration (NASA) with the grant numbers of NNX16AN21A and NNX12C21A, and National Science Foundation (NSF) under award numbers of CMMI-1762353, CMMI-1824840 and CBET-1435590.

References

[1] S. Farhadi, M. Farzaneh, S.A. Kulinich, Anti-icing performance of superhydrophobic surfaces, Appl. Surf. Sci. 257 (2011) 6264–6269, https://doi.org/10.1016/j.apsusc.2011.02.057.
[2] O. Parent, A. Ilinca, Anti-icing and de-icing techniques for wind turbines: critical review, Cold Reg. Sci. Technol. 65 (2011) 88–96, https://doi.org/10.1016/j.coldregions.2010.01.005.
[3] Y. Liu, L. Ma, W. Wang, A.K. Kota, H. Hu, An experimental study on soft PDMS materials for aircraft icing mitigation, Appl. Surf. Sci. 447 (2018) 599–609, https://doi.org/10.1016/J.APSUSC.2018.04.032.
[4] W. Dong, J. Zhu, M. Zheng, G.L. Lei, Z.X. Zhou, Experimental study on icing and anti-icing characteristics of engine inlet guide vanes, J. Propuls. Power 31 (2015) 1330–1337, https://doi.org/10.2514/1.B35679.
[5] Y. Liu, C. Kolbakir, H. Hu, H. Hu, A comparison study on the thermal effects in DBD plasma actuation and electrical heating for aircraft icing mitigation, Int. J. Heat Mass Transf. 124 (2018) 319–330, https://doi.org/10.1016/J.IJHEATMASSTRANSFER.2018.03.076.
[6] S.K. Thomas, R.P. Cassoni, C.D. MacArthur, Aircraft anti-icing and de-icing techniques and modeling, J. Aircr. 33 (1996) 841–854, https://doi.org/10.2514/3.47027.
[7] M. Pourbagian, W.G. Habashi, Aero-thermal optimization of in-flight electro-thermal ice protection systems in transient de-icing mode, Int. J. Heat Fluid Flow 54 (2015) 167–182, https://doi.org/10.1016/j.ijheatfluidflow.2015.05.012.
[8] O. Fakorede, H. Ibrahim, A. Ilinca, J. Perron, Experimental investigation of power requirements for wind turbines electrothermal anti-icing systems, Wind Turbines-Des. Control Appl, 2016, https://doi.org/10.5772/63449.
[9] W. Dong, J. Zhu, M. Zheng, Y. Chen, Thermal analysis and testing of nonrotating cone with hot-air anti-icing system, J. Propuls. Power (2015) 1–8, https://doi.org/10.2514/1.B35378.
[10] P. Tourkine, M. Le Merrer, D. Quéré, Delayed freezing on water repellent materials, Langmuir 25 (2009) 7214–7216, https://doi.org/10.1021/la900929u.
[11] P. Bizi-Bandoki, S. Benayoun, S. Valette, B. Beaugiraud, E. Audouard, Modifications of roughness and wettability properties of metals induced by femtosecond laser treatment, Appl. Surf. Sci. 257 (2011) 5213–5218, https://doi.org/10.1016/j.apsusc.2010.12.089.
[12] A. Cunha, A.P. Serro, V. Oliveira, A. Almeida, R. Vilar, M.C. Durrieu, Wetting behaviour of femtosecond laser textured Ti-6Al-4V surfaces, Appl. Surf. Sci. 265 (2013) 688–696, https://doi.org/10.1016/j.apsusc.2012.11.085.
[13] M.V. Rukosuyev, J. Lee, S.J. Cho, G. Lim, M.B.G. Jun, One-step fabrication of superhydrophobic hierarchical structures by femtosecond laser ablation, Appl. Surf. Sci. 313 (2014) 411–417, https://doi.org/10.1016/j.apsusc.2014.05.224.
[14] A.Y. Vorobyev, C. Guo, Multifunctional surfaces produced by femtosecond laser pulses, J. Appl. Phys. 117 (2015), https://doi.org/10.1063/1.4905616.
[15] R. Jagdheesh, M. Diaz, J.L. Ocaña, Bio inspired self-cleaning ultrahydrophobic aluminium surface by laser processing, RSC Adv. 6 (2016) 72933–72941, https://doi.org/10.1039/C6RA12236A.
[16] B.H. Luo, P.W. Shum, Z.F. Zhou, K.Y. Li, Preparation of hydrophobic surface on steel by patterning using laser ablation process, Surf. Coatings Technol. 204 (2010) 1180–1185, https://doi.org/10.1016/j.surfcoat.2009.10.043.
[17] M.H. Kwon, H.S. Shin, C.N. Chu, Fabrication of a super-hydrophobic surface on metal using laser ablation and electrodeposition, Appl. Surf. Sci. 288 (2014) 222–228, https://doi.org/10.1016/j.apsusc.2013.10.011.
[18] D. Framil Carpeño, M. Dickinson, C. Seal, M. Hyland, Induced hydrophobicity in micro- and nanostructured nickel thin films obtained by ultraviolet pulsed laser treatment, Phys. Status Solidi Appl. Mater. Sci. 213 (2016) 2709–2713, https://doi.org/10.1002/pssa.201600101.
[19] B. Wu, M. Zhou, J. Li, X. Ye, G. Li, L. Cai, Superhydrophobic surfaces fabricated by microstructuring of stainless steel using a femtosecond laser, Appl. Surf. Sci. 256 (2009) 61–66, https://doi.org/10.1016/j.apsusc.2009.07.061.
[20] T. Chen, H. Liu, H. Yang, W. Yan, W. Zhu, H. Liu, Biomimetic fabrication of robust self-assembly superhydrophobic surfaces with corrosion resistance properties on stainless steel substrate, RSC Adv. 6 (2016) 43937–43949, https://doi.org/10.1039/C6RA06500G.
[21] M.K. Tang, X.J. Huang, Z. Guo, J.G. Yu, X.W. Li, Q.X. Zhang, Fabrication of robust and stable superhydrophobic surface by a convenient, low-cost and efficient laser marking approach, Colloids Surfaces A Physicochem. Eng. Asp. 484 (2015) 449–456, https://doi.org/10.1016/j.colsurfa.2015.08.029.
[22] B. Li, H. Li, L. Huang, N. Ren, X. Kong, Femtosecond pulsed laser textured titanium surfaces with stable superhydrophilicity and superhydrophobicity, Appl. Surf. Sci. 389 (2016) 585–593, https://doi.org/10.1016/j.apsusc.2016.07.137.
[23] D.M. Chun, C.V. Ngo, K.M. Lee, Fast fabrication of superhydrophobic metallic surface using nanosecond laser texturing and low-temperature annealing, CIRP Ann. - Manuf. Technol. 65 (2016) 519–522, https://doi.org/10.1016/j.cirp.2016.04.019.

[24] H. Ding, Q. Wang, A. Samanta, N. Shen, Nanosecond Laser-based High-throughput Surface Nano-Structuring (nHSN) Process, US20190054571A1, https://patents.google.com/patent/US20190054571A1/en, (2019) (accessed May 29, 2019).
[25] A. Samanta, Q. Wang, S.K. Shaw, H. Ding, Nanostructuring of laser textured surface to achieve superhydrophobicity on engineering metal surface, J. Laser Appl. 31 (2019) 22515, , https://doi.org/10.2351/1.5096148.
[26] Q. Wang, A. Samanta, F. Toor, S. Shaw, H. Ding, Colorizing Ti-6Al-4V surface via high-throughput laser surface nanostructuring, J. Manuf. Process. (2019), https://doi.org/10.1016/J.JMAPRO.2019.03.050.
[27] L. Cao, A.K. Jones, V.K. Sikka, J. Wu, D. Gao, Anti-icing superhydrophobic coatings, Langmuir 25 (2009) 12444–12448, https://doi.org/10.1021/la902882b.
[28] E.A. Bogoslov, M.P. Danilaev, S.A. Mikhailov, Y.E. Pol'skii, Energy efficiency of an integral anti-ice system based on fluoroplastic films, J. Eng. Phys. Thermophys. 89 (2016) 815–820, https://doi.org/10.1007/s10891-016-1441-5.
[29] M. Ruan, W. Li, B. Wang, B. Deng, F. Ma, Z. Yu, Preparation and anti-icing behavior of superhydrophobic surfaces on aluminum alloy substrates, Langmuir 29 (2013) 8482–8491, https://doi.org/10.1021/la400979d.
[30] L.B. Boinovich, A.M. Emelyanenko, K.A. Emelyanenko, K.I. Maslakov, Anti-icing properties of a superhydrophobic surface in a salt environment: an unexpected increase in freezing delay times for weak brine droplets, Phys. Chem. Chem. Phys. 18 (2016) 3131–3136, https://doi.org/10.1039/C5CP06988B.
[31] A.J. Meuler, J.D. Smith, K.K. Varanasi, J.M. Mabry, G.H. McKinley, R.E. Cohen, Relationships between water wettability and ice adhesion, ACS Appl. Mater. Interfaces 2 (2010) 3100–3110, https://doi.org/10.1021/am1006035.
[32] R.N. Wenzel, Resistance of solid surfaces to wetting by water, Ind. Eng. Chem. 28 (1936) 988–994, https://doi.org/10.1021/ie50320a024.
[33] N. Shen, H. Ding, Q. Wang, H. Ding, Effect of confinement on surface modification for laser peen forming without protective coating, Surf. Coatings Technol. 289 (2016) 194–205, https://doi.org/10.1016/J.SURFCOAT.2016.01.054.
[34] M.C. Gupta, B.K. Nayak, Systems and Methods of Laser Texturing of Material Surfaces and Their Applications, US8846551 B2 (2010).
[35] C. Guo, A.Y. Vorobyev, Super-hydrophobic Surfaces and Methods for Producing Super-hydrophobic Surfaces, US 2015/0136226 A1, (2015) (doi:US 2013/0154292 A1).
[36] A. Steele, K.N. Barada, D. Alexander, C.G. Mool, L. Eric, Linear abrasion of a titanium superhydrophobic surface prepared by ultrafast laser microtexturing, J. Micromechanics Microengineering. 23 (2013) 115012, , https://doi.org/10.1088/0960-1317/23/11/115012.
[37] R. Jagdheesh, B. Pathiraj, E. Karatay, G.R.B.E. Römer, A.J. Huis In'T Veld, Laser-induced nanoscale superhydrophobic structures on metal surfaces, Langmuir 27 (2011) 8464–8469, https://doi.org/10.1021/la2011088.
[38] B. Liu, W. Wang, G. Jiang, X. Mei, Z. Wang, K. Wang, J. Cui, Study on hierarchical structured PDMS for surface super-hydrophobicity using imprinting with ultrafast laser structured models, Appl. Surf. Sci. 364 (2016) 528–538, https://doi.org/10.1016/j.apsusc.2015.12.190.
[39] C. Dorrer, J. Rühe, Some thoughts on superhydrophobic wetting, Soft Matter 5 (2009) 51, https://doi.org/10.1039/b811945g.
[40] J.W. Drelich, L. Boinovich, E. Chibowski, C. Della Volpe, L. Hołysz, A. Marmur, S. Siboni, Contact angles: history of over 200 years of open questions, Surf. Innov. (2019) 1–25, https://doi.org/10.1680/jsuin.19.00007.
[41] J.W. Drelich, Contact angles: from past mistakes to new developments through liquid-solid adhesion measurements, Adv. Colloid Interf. Sci. 267 (2019) 1–14, https://doi.org/10.1016/j.cis.2019.02.002.
[42] V.J. Rico, C. López-Santos, M. Villagrá, J.P. Espinós, G.F. de la Fuente, L.A. Angurel, A. Borrás, A.R. González-Elipe, Hydrophobicity, freezing delay, and morphology of laser-treated aluminum surfaces, Langmuir 35 (2019) 6483–6491, https://doi.org/10.1021/acs.langmuir.9b00457.
[43] L.B. Boinovich, A.M. Emelyanenko, K.A. Emelyanenko, E.B. Modin, *Modus operandi* of protective and anti-icing mechanisms underlying the design of longstanding outdoor icephobic coatings, ACS Nano 13 (2019) 4335–4346, https://doi.org/10.1021/acsnano.8b09549.
[44] A. Ganne, K.I. Maslakov, A.I. Gavrilov, Anti-icing properties of superhydrophobic stainless steel mesh at subzero temperatures, Surf. Innov. 5 (2017) 154–160, https://doi.org/10.1680/jsuin.17.00026.
[45] L.B. Boinovich, K.A. Emelyanenko, A.G. Domantovsky, A.M. Emelyanenko, Laser tailoring the surface chemistry and morphology for wear, scale and corrosion resistant superhydrophobic coatings, Langmuir 34 (2018) 7059–7066, https://doi.org/10.1021/acs.langmuir.8b01317.
[46] R.M. Waldman, H. Li, H. Hu, An experimental investigation on the effects of surface wettability on water runback and ice accretion over an airfoil surface, 8th AIAA Atmos. Sp. Environ. Conf, American Institute of Aeronautics and Astronautics, Virginia, 2016, , https://doi.org/10.2514/6.2016-3139.
[47] Y. Liu, L. Li, H. Li, H. Hu, An experimental study of surface wettability effects on dynamic ice accretion process over an UAS propeller model, Aerosp. Sci. Technol. 73 (2018) 164–172, https://doi.org/10.1016/j.ast.2017.12.003.
[48] L. Xu, W.W.W. Zhang, S.R.S. Nagel, Drop splashing on a dry smooth surface, Phys. Rev. Lett. 94 (2005) 184505, , https://doi.org/10.1103/PhysRevLett.94.184505.
[49] L. Ma, H. Li, H. Hu, An experimental study on the dynamics of water droplets impingement onto a goose feather, 55th AIAA Aerosp. Sci. Meet, American Institute of Aeronautics and Astronautics, Reston, Virginia, 2017, , https://doi.org/10.2514/6.2017-0442.
[50] D. Khojasteh, M. Kazerooni, S. Salarian, R. Kamali, Droplet impact on superhydrophobic surfaces: a review of recent developments, J. Ind. Eng. Chem. 42 (2016) 1–14, https://doi.org/10.1016/J.JIEC.2016.07.027.
[51] A. Work, Y. Lian, A critical review of the measurement of ice adhesion to solid substrates, Prog. Aerosp. Sci. (2018), https://doi.org/10.1016/j.paerosci.2018.03.001.
[52] S.A. Kulinich, M. Farzaneh, How wetting hysteresis influences ice adhesion strength on superhydrophobic surfaces, Langmuir 25 (2009) 8854–8856, https://doi.org/10.1021/la901439c.
[53] S.A. Kulinich, M. Honda, A.L. Zhu, A.G. Rozhin, X.W. Du, The icephobic performance of alkyl-grafted aluminum surfaces, Soft Matter 11 (2015) 856–861, https://doi.org/10.1039/C4SM02204A.